The range of Jupiter's flow structures fitting the Juno asymmetric gravity measurements

Keren Duer[1], Eli Galanti[1] and Yohai Kaspi[1]

(JGR planets, in rev.)

May 5, 2020

[1]*Department of Earth and Planetary Sciences, Weizmann Institute of Science, Rehovot, Israel.*

Abstract

The asymmetric gravity field measured by the Juno spacecraft allowed estimation of the depth of Jupiter's zonal jets, showing that the winds extend approximately 3000 km beneath the cloud-level. This estimate was based on an analysis using a combination of all measured odd gravity harmonics J_3, J_5, J_7, and J_9, but the wind profile dependence on each of them separately has not been investigated. Furthermore, these calculations assumed the meridional profile of the cloud-level wind extends to depth. However, it is possible that the interior jet profile varies from that of the cloud-level as hinted by the Juno microwave measurement that find a smoother nadir brightness temperature profile at depth compared to the cloud-level. Here we analyze in detail the possible meridional and vertical structure of Jupiter's deep jet-streams. We find that each odd gravity harmonic constrains the flow at a different depth, with J_3 being the most dominant at depths below 3000 km, J_5 being the most restrictive overall, and J_9 not constraining the flow at all if the other odd harmonics are within the measurement range. Interior flow profiles constructed from perturbations to the cloud-level winds allow a more extensive range of vertical wind profiles, yet when the profiles differ substantially from the cloud-level, the ability to match the gravity data reduces significantly. Overall, we find that while interior wind profiles that do not resemble the cloud-level are possible, they are statistically unlikely. However, slightly smoother profiles, which resemble the Juno's microwave radiometer temperature profile at depth, are still compatible with the gravity measurements.

Plain Language Summary

Jupiter's north-south asymmetric gravity field that was measured by the Juno spacecraft, currently orbiting Jupiter, allowed estimating the depth of the jet-streams (associated with the famous visible cloud bands) to approximately $\sim$ 3000 km. This estimate was based on all the gravity field measurements combined, however, there is also information about the structure of the flow hidden in each measurement alone. Here we analyze those measurements and show how each of them constrains the flow at a different depth. We also systematically investigate the statistical likelihood of wind profiles that differ from the profile observed at the cloud-level with various structures at depth. We find that for Jupiter's measured cloud-level jet streams, only a relatively narrow envelope of vertical structures allow fitting the gravity data. Although other jet profiles that are different from the observed at the cloud-level are feasible (still consistent with the gravity data), they are statistically unlikely. Finally, we explore depth-dependent wind structure inspired by the Juno microwave radiometer instrument, which indicates that the ammonia abundance varies with depth and might be correlated to the jet-streams. We find that such a profile can still match the gravity data as long as the variation from the cloud-level wind is not substantial.

1 Introduction

The Juno spacecraft has provided an unprecedented glance into Jupiter's atmospheric flows below the cloud-level. The high precision gravity measurements, particularly the odd gravitational harmonics repeated in multiple passes

(Iess et al., 2018), presented an opportunity to estimate the depth and structure of Jupiter's zonal jets. It was found that the zonal jets are deep and penetrate to approximately 3000 km below the cloud-level (Kaspi et al., 2018). Below this depth, the even gravitational harmonics indicate that Jupiter is rotating nearly as a solid body (Guillot et al., 2018). However, determining the details of the decay profile with depth poises a significant challenge. There appear to be remnants of the zonal flows even below 4000 km, and since the estimation for the electrical conductivity in Jupiter at this depth is at least ~ 10 S m^{-1} (Nellis et al., 1996; Wicht et al., 2019b,a), an interaction between the flow and the magnetic field is expected there (Cao and Stevenson, 2017; Galanti et al., 2017a; Duer et al., 2019; Moore et al., 2019). Understanding the gravity harmonic signature and the flow structure below the cloud-level is thus essential to complete the picture.

The gravity field of Jupiter reflects both its internal density structure and the zonal flow structure (Hubbard, 1999; Kaspi et al., 2010). The even gravity harmonics are used to constrain the internal density structures of Jupiter and other gas giants (e.g., Hubbard et al., 1974; Hubbard et al., 1975; Helled et al., 2010; Nettelmann et al., 2013). Multiple studies showed that the higher-order (even) gravity harmonics are sensitive to the outer regions of the planet (e.g., Zharkov and Trubitsyn, 1974; Guillot and Gautier, 2007; Nettelmann et al., 2013). Their exact value is defined by the density distribution throughout the planet and the planet's rotation, composition, shape, mass, and radius. Since for a static gas planet, the odd harmonics are identically zero, any gravitational asymmetry between north and south would indicate on a dynamical source generating those asymmetries (Kaspi, 2013). Juno measured with high precision the gravity harmonics up to J_{10}, including significant odd values. The measured values and error range are: $J_3\left(\times 10^{-8}\right) = -4.24 \pm 0.91$, $J_5\left(\times 10^{-8}\right) = -6.89 \pm 0.81$, $J_7\left(\times 10^{-8}\right) = 12.39 \pm 1.68$ and $J_9\left(\times 10^{-8}\right) = -10.58 \pm 4.35$ (Iess et al., 2018). The relation between the density anomaly and the flow (thermal wind balance) allows constraining the deep flow structure within the planet (Kaspi et al., 2010; Kaspi, 2013; Kaspi et al., 2018). Assuming that the cloud-level zonal wind structure is extended towards Jupiter's interior using a scaling factor, one can find many solutions for the deep flow structure that satisfy all four odd gravity harmonics within the uncertainty range. With the currently available data, Jupiter's deep flow cannot be determined uniquely (Kaspi et al., 2018; Kong et al., 2018), and systematic exploration of the range of the deep flow structure is necessary.

Moreover, the meridional structure of the zonal wind is not necessarily constant with depth. The cloud-level wind itself has a measurement error (Garcıa-Melendo and Sánchez-Lavega, 2001; Salyk et al., 2006; Tollefson et al., 2017), and as it extends inward the profile might vary, although any such variation must be accompanied with a meridional temperature gradient as well. Some evidence for such meridional variations come from the Juno microwave radiometer (MWR) measurements showing that the nadir brightness temperature profile (dominated by the ammonia abundance), becomes smoother with depth (Bolton et al., 2017; Li et al., 2017). Although this measurement is not necessarily correlated with temperature, it does coincide to some degree with the zonal wind profile at the cloud-level (Bolton et al., 2017), and thus might provide a hint to the vertical variation of the zonal wind profile in the upper 300 km.

Previous work on constraining the deep flow structure was done using all four measured gravity harmonics combined (e.g., Kaspi et al., 2018; Kong et al., 2018). However, an important question is how each gravity harmonic individually constrains the flow strength at different depths. Here, we examine the individual contribution of each odd gravity harmonic, with emphasis on the depth of influence and the relation to the cloud-level zonal wind profile. In order to provide a systematic analysis we take a hierarchal approach where we increase the level of complexity of the variation of the wind structure, and in all cases explore what is the range of solutions that match the gravity measurements. We begin with solutions which are identical to the cloud-level profile, and allow only for the vertical decay to vary. Then, we relax the constraint on the meridional profile of the zonal wind, and allow variations to the measured cloud-level profile along with the varying vertical decay. Finally, we examine random meridional profiles that are not related at all to Jupiter's measured cloud-level profile, exploring the possibility that the interior wind structure, which is influencing the gravity measurements, is completely different than the cloud-level flow. Following this logic, we also search for solutions with smoother wind profiles at depth, resembling the MWR measurements at 300 km (channel 1), and calculate the vertical structure of such flows that can match also the gravity data.

The paper is structured as follows: in section 2 we introduce the theoretical background for this analysis, connecting the gravity measurements and the wind profile. In section 3 we present the possible solutions for Jupiter's wind structure, the depth sensitivity obtained by excluding a specific harmonic, and the contribution function of each harmonic. In section 4 we discuss the ability to find solutions for the anomalous gravity field of different meridional arrangements and in section 5 we explore depth-dependent meridional structures, inspired by the MWR measurements. Finally, in section 6 we discuss the significance and conclusions of this study.

2 Methodology

The density distribution within Jupiter is reflected in the zonal gravity harmonics (J_n), which describe the external gravitational field of the planet in equilibrium (Zharkov and Trubitsyn, 1974). The gravity harmonics can be represented by

$$J_n = -\frac{1}{MR_J^n}\int \rho r^n P_n d^3r, \tag{1}$$

where M and R_J are Jupiter's mass and equatorial radius, respectively, n is the harmonic degree ($n = 2, ..., N$), ρ is density, r is the radial coordinate and P_n is the n-th Legendre polynomial (Hubbard, 1984). The density can be decomposed such that $\rho(r,\theta) = \widetilde{\rho}(r,\theta) + \rho'(r,\theta)$, where $\widetilde{\rho}(r,\theta)$ is the static component that is determined by the planet's shape and rotation (Hubbard, 2012), and $\rho'(r,\theta)$ is the dynamical anomaly representing fluid velocities with respect to the solid body rotation with θ being latitude (Kaspi et al., 2010). The zonal gravity harmonics that represent only the dynamical part of the flow (ΔJ_n) can be calculated by integrating the density anomaly and its projection onto the Legendre polynomials in spherical coordinates such that

$$\Delta J_n = -\frac{2\pi}{MR_J^n}\int_0^{R_J}\int_{-1}^{1}\rho'(r,\mu)\, r^{n+2} P_n(\mu)\, d\mu dr, \tag{2}$$

where $\mu = r\sin\theta$. Since an oblate planet with no dynamics is symmetric between north and south, the density anomaly represented by the odd harmonics ($n = 3, 5, ..$) should be identically zero if the flow pattern is symmetric or if the dynamics are shallow ($\Delta J_n = J_n$ for odd n). However, Juno measured four odd gravity harmonics (Iess et al., 2018), indicating a strong asymmetric pattern exists in Jupiter's flow field and on the existence of strong and deep winds.

The rapid rotation and size of the planet (small Rossby number) imply that this asymmetry can be directly related to zonal flows, since to first order, the leading balance in Jupiter is a geostrophic balance between the flow related Coriolis forces and the pressure gradients. This leads to a vorticity balance known as thermal wind balance (Pedlosky, 1987; Kaspi et al., 2009). If only zonal (azimuthal) flows are considered, thermal wind balance can be written as

$$2\Omega r\frac{\partial(\tilde{\rho}u)}{\partial z} = g_0\frac{\partial\rho'}{\partial\theta}, \tag{3}$$

where Ω is Jupiter's rotation rate, $u(r,\theta)$ is the zonal flow, $g_0(r)$ is the mean gravitational acceleration and z is the direction parallel to the rotation axis. An equivalent equation can be written with temperature instead of density gradients, and one can easily switch between the two versions (Kaspi et al., 2016). Galanti et al. (2017b) showed that a higher order expansion, beyond thermal wind, provides only a small (less than 10%) correction for determining the deep flow dynamics, and therefore, for the purpose of studying the overall vertical structure, it can be neglected.

Our goal here is to search for possible deep wind structures that can explain each one of the measured odd gravity harmonics (J_3, J_5, J_7, and J_9). Unlike previous studies (e.g., Kaspi et al., 2018), we are not solving for an optimal solution with respect to the full error covariance matrix. Any vertical wind structure that fits the odd measured gravity harmonics, within the uncertainty range of Juno, is considered a possible solution for the flow. This allows to examine the full range of possible solutions, without converging to a single decay structure of the flow. For example, the solution suggested by Kaspi et al. (2018) that considered the error covariance matrix is not a solution here since the value of J_3 is not within the measured error.

3 The range of the zonal flows vertical profile

Taking a hierarchal approach, with an increasing level of complexity, we first use the observed cloud-level wind as an upper boundary condition for the flow field and assume the same profile continues inward in a direction parallel to the spin axis, due to angular momentum considerations (Busse, 1976; Kaspi et al., 2010). The possible deep flow structures are set to decay continuously from the cloud-level to few thousands of kilometers (Kaspi et al., 2018), using two different decay regions. The choice to divide the decay functions into two distinct regions rises from the possible magnetic field effects on the flow, expected at $r < 0.97\,R_J$ (Duer et al., 2019; Wicht et al., 2019b), which imply that once the electrical conductivity begins to be dominant the magnetic field acts to dissipate the flow (Liu

et al., 2008; Gastine et al., 2014). Thus, for the lower part (the semiconducting region), we choose an exponential decay (Eq. 6) that fits the exponential nature of the electrical conductivity within Jupiter (Nellis et al., 1992; Weir et al., 1996; French et al., 2012). For the upper part, the function includes both an exponent and hyperbolic tangent (Eq. 5), which combine to give a wide possible range of decay functions.

The vertical structure of the zonal flow is defined with six independent parameters, chosen to cover an extensive range of vertical structures. It is set as

$$u(\theta, r) = u_{\mathrm{proj}}(\theta, r) Q_s(r), \tag{4}$$

$$Q_s(r) = (1-\alpha)\exp\left(\frac{r-R_J}{H_1}\right) + \alpha\left[\frac{\tanh\left(-\frac{R_J-H_2-r}{\Delta H}\right)+1}{\tanh\left(\frac{H_2}{\Delta H}\right)+1}\right] \qquad R_T \le r \le R_J, \tag{5}$$

$$Q_s(r) = Q_s(R_T)\exp\left(\frac{r-R_T}{H_3}\right) \qquad r < R_T, \tag{6}$$

where $u_{\mathrm{proj}}(r,\theta)$ is the wind at the cloud-level, projected inwards (with no decay) in the direction parallel to the axis of rotation ($\hat{z}$ axis, Eq. 3), $Q_s(r)$ is the radial decay function, representing the fraction of the cloud-level wind at every depth, and the set of parameters that forms the decay are bounded in the following limits: $0 \le \alpha \le 1$, $200 \le H_1,\ H_2\ , \Delta H \le 2500$ km, $0.95 \le R_T \le 0.975\, R_J$ and $100 \le H_3 \le 900$ km. The function Q_s is also smoothed at the transition depth. From each set of systematically random chosen parameters (the parameters are spaced uniformly between the bounds), we calculate the resulting density anomaly and the implied odd gravity harmonics. This process is repeated for all possible combinations of parameters, (5×10^5 cases) to sufficiently cover the parameter space. The only requirement we make is that all cases will be monotonically decreasing. All decay options are considered as the sample population for this study, and all the calculations presented below are performed using the same set of functions. Note that other forms of Q_s are possible, and can still fit the measured gravity data ($Q_S(r,\theta)$ for example), however for the exploration of the individual gravity harmonic depth sensitivity and the meridional profile anomalies, we find that the chosen function, which allows a very wide range of decay profiles, is satisfactory.

From the 5×10^5 decay options examined, 6712 vertical structures are compatible with Juno's measured odd gravity harmonics, which represent a little over 1% of the sample population (Fig. 1a). All of the compatible decay structures lay in a relatively narrow envelope, especially in the region around 2000 km depth and below 4000 km, and all the options are pointing to remnants of jet-associated velocities at 4000 km (Fig. 1). Those deep velocities are still at the order of 1 m s^{-1} and despite being small, they are still higher than the magnetic secular variation associated velocities estimates by Moore et al. (2019). Increasing the error range of Juno's gravity measurements does allow for more solutions, but the overall structure does not change much (Fig. 1b).

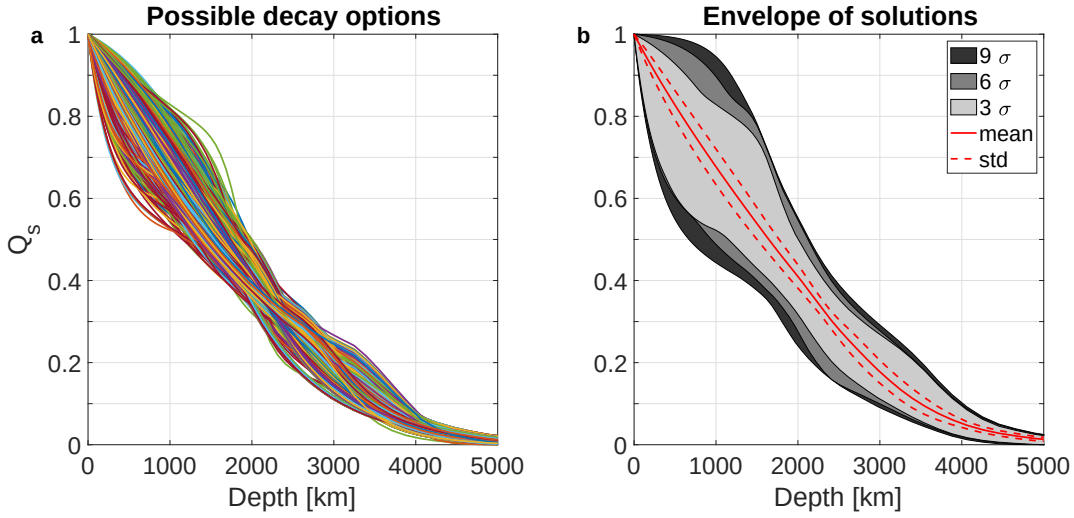

Figure 1: (a) Decay options that fit all four measured odd gravity harmonics (J_n) within the 3σ sensitivity range of Juno, using Jupiter's observed cloud-level flows (Tollefson et al., 2017). (b) Envelope of all possible solutions (light gray), the average solution of all options (red line), their standard deviation (dashed red lines) and envelope of solutions satisfying larger uncertainty range (darker gray with rising uncertainty range).

3.1 The depth sensitivity of the odd harmonics

Research to date focused on finding vertical profiles that match all four gravity harmonics. However, there is information to be obtained from each gravity harmonic separately. Here, vertical flow profiles that fit three out of the four measured odd gravity harmonics are considered, and the depth sensitivity of the excluded harmonic is studied by examining the difference between the vertical profiles that include the specific J_n to those that do not necessarily include it. The resulting depth sensitivity of each odd measured gravity harmonic, according to Jupiter's measured zonal profile, is presented in Fig. 2. The gray envelope, the same envelope from Fig. 1b, is the boundary of all possible solutions that fit all four odd gravity harmonics within 3σ. Note that not all lines inside the gray envelope will necessarily generate a solution compatible with the measured gravity field, since the solution is also dependent on the decay profile within the given envelope. All additional solutions that are gained while excluding one of the odd gravity harmonics appears in Fig. 2 (cyan envelopes). The cyan envelopes always contain the gray envelope by definition, since they are constructed by fitting at least three gravity harmonics. The difference between the cyan envelopes and the gray ones emphasizes the region in which the *excluded* harmonic bounds the flow.

The most insignificant influence is clearly of J_9 (Fig. 2d). It appears to add no solutions at all to the gray envelope, meaning, J_9 does not constrain the flow *if* the other three odd values are still within Juno's 3σ. This is likely because J_9 has the highest measurement error, and lowest signal to noise ratio (SNR), so even while fitting J_9, there is an extensive region of solutions, and excluding it does not add new solutions. The largest influence on flow structure and depth sensitivity, comes from J_5 (Fig. 2b). It appears to set the upper boundary of the gray envelope from the cloud level (0 km) to 3500 km, and a lower boundary of the gray envelope between 2000 to 3500 km. The strongest sensitivity is between the cloud level and 3000 km. J_5 has the smallest measured 3σ value, and the largest SNR, however its value is very similar to the SNR of J_7 thus the large influence of J_5 cannot be a result of the SNR alone. In a similar manner, J_3 is mostly sensitive between 3000 and 5000 km and between the cloud level (0 km) to 1500 km (Fig. 2a). Note that a flow structure that decays to zero at 4000 km ($\sim 0.94\,R_J$) can not fit J_3. J_7 is sensitive between 500 and 2500 km, and sets mainly the lower boundary of the gray envelope at those depths (Fig. 2c). As expected from the gravity harmonics equation, the odd harmonics, similarly to the even harmonics depth sensitivity, show that higher order harmonics are more sensitive in outer regions (Zharkov and Trubitsyn, 1974; Guillot and Gautier, 2007; Nettelmann et al., 2013). However, the depth dependence is more complicated when addressing the odd harmonics.

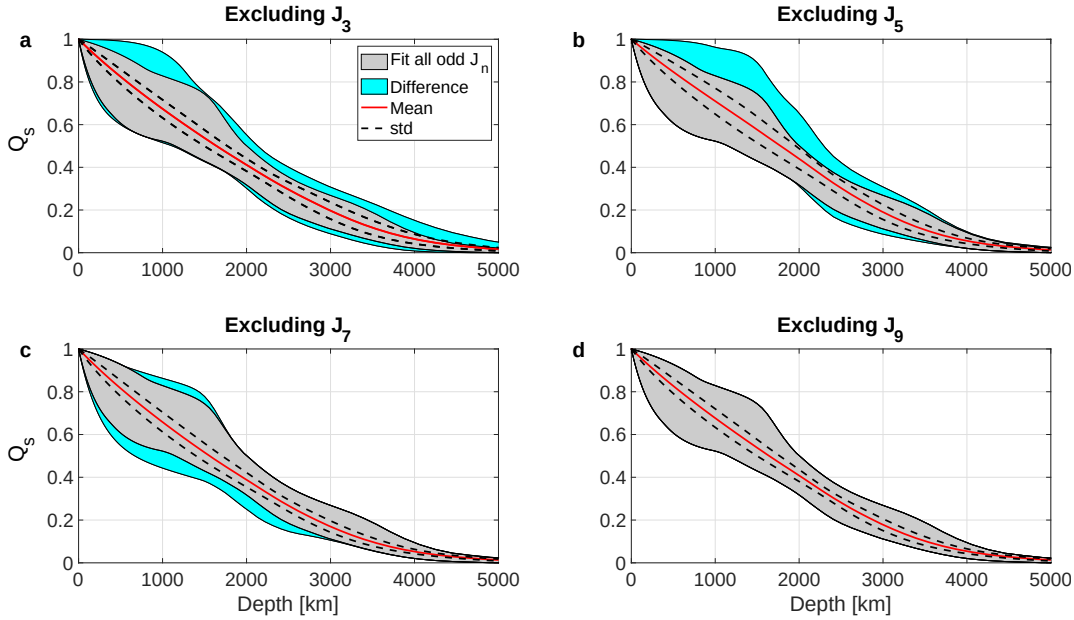

Figure 2: (a) The envelope of possible solutions that fit all four odd gravity harmonics (gray), the envelope of additional solutions once excluding J_3 (while still fitting J_5, J_7 and J_9) (cyan), the average of all decay options within the subplot (gray and cyan combined) (red), and the standard deviation of them (dashed black). The other panels are the same while excluding other J_n: (b) excluding J_5, (c) excluding J_7 and (d) excluding J_9. The results are a combination of the sample decay options (5×10^5). Note that the cyan color emphasizes the depth sensitivity of each gravity harmonic separately.

3.2 Contribution function

The depth sensitivity of the gravity harmonics can also be examined by calculating directly the depth dependence of J_n, defined as the contribution function. This function was calculated in past studies for the even harmonics of Jupiter and other planets (e.g., Guillot and Gautier, 2007; Helled et al., 2010; Nettelmann et al., 2013). The contribution of each shell is basically the normalized integrant of J_n, defined as

$$C_n = \frac{1}{J_n}\frac{dJ_n}{dr} = \frac{1}{J_n}\frac{-2\pi}{MR_J^n}\int_{-1}^{1}\rho\left(r,\mu\right)r^{n+2}P_n\left(\mu\right)d\mu \tag{7}$$

(Zharkov and Trubitsyn, 1974; Hubbard et al., 1974; Hubbard, 1984). The even harmonics in past studies were calculated from the background density (solid body models), while in our study we use the wind-induced anomalous density field to calculate the odd harmonics contribution, so here $\rho = \rho'$.

The averaged anomalous density profile of all possible decay structures, that are consistent with all four odd gravity harmonics, is presented in Fig. 3a. The anomalous density reveals a change of sign at 2000 km. The averaged odd contribution functions (C_n) and standard deviations of each odd gravity harmonic (Fig. 3b) corresponding to the solution envelope from Fig. 1, show a consistent sign change. The change of sign is exhibited only by the anomalous density, and therefore, does not exist when examining the static density resulting even harmonics (e.g., Nettelmann et al., 2013). The integrals of the non-normalized contribution curve are the gravity harmonic values (J_n), so the sign and the value of J_n is set by the difference between the positive and negative curves (above and below 2000 km). For the averaged anomalous density, the gravity harmonics are: $J_3\left(\times 10^{-8}\right) = -4.29$, $J_5\left(\times 10^{-8}\right) = -7.50$, $J_7\left(\times 10^{-8}\right) = 10.8$ and $J_9\left(\times 10^{-8}\right) = -6.69$.

The contribution function reveals a complex depth dependence for all four values. The depth sensitivity of each contribution function is pronounced by the triangles (Fig. 3b), which represent the depth of the mean absolute anomaly. C_3, which has the largest contribution from both the upper and lower regions, gets more contribution from the lower part, according to the depth of the mean anomaly which here equals 2020 km (Fig. 3b, blue triangle), meaning the curve below 2000 km is larger than the curve above this depth. The standard deviation of C_3 (Fig. 3b, blue shading) is the largest, implying on large variability of the solutions with depth when considering the J_3 value. C_5 depends mostly on the deeper part of the density anomaly (Fig. 3b, red triangle). This might explain the strong depth sensitivity of J_5 revealed in Fig. 3, however, the standard deviation of C_5 is substantial only between 2000 and 4000 km. C_7 and C_9 clearly depend much more on the upper part (yellow and green triangles $<$ 2000 km) and their standard deviation is small everywhere. It is evident that the contribution function of the odd harmonics exhibits a more complicated pattern than the classical even harmonics (e.g., Guillot and Gautier, 2007; Helled et al., 2010; Nettelmann et al., 2013). Unlike the even harmonics, which correspond mostly to the static shape of the planet, the higher odd harmonics are not simply more pronounced in the outer regions. The projection of the wind patterns onto different depths is reflected in the odd harmonics contribution in those depths, suppressing the $\left(r/R_J\right)^n$ dependency, which is the prominent feature for the even harmonics contribution.

4 Sensitivity to the meridional profile of the zonal flows

Next, we aim to question the assumption that the meridional profile of Jupiter's zonal flow remains constant at all depths, which we have used in the previous section (3). First, the zonal wind profile is measured by tracking of cloud motions, which itself has some uncertainty (Tollefson et al., 2017), and second, and most importantly, the assumption that the cloud-level profile extends perfectly to depth requires the flow to be locally closer-to-barotropic (in the upper few thousands of kilometers), which is not necessarily the case. Although the flow cannot be completely barotropic if $Q_s \neq 1$ (Eq. 4), the horizontal temperature gradients required to balance such changes can be small (Eq. 3). On the other hand, any deviation from close-to-barotropic flow must be supported by large horizontal temperature gradients, which themselves must be maintained by some internal mechanism (Showman and Kaspi, 2013). Internal convection models support the scenario that there may be internal shear over the upper few thousand kilometers, but the overall structure of the flow does not change much (Kaspi et al., 2009; Jones and Kuzanyan, 2009). Any significant deviation from the zonal wind structure observed at the cloud level requires significant shear and therefore significant horizontal thermal gradients (thermal-wind balance). As this is an open question, for the purpose of this analysis we examine several cases of zonal wind meridional profiles, under the assumption that the wind structure possibly varies close to the cloud level and then projects inward without further modifications. For the purpose of the gravity analysis this means that the altered meridional profiles occupies

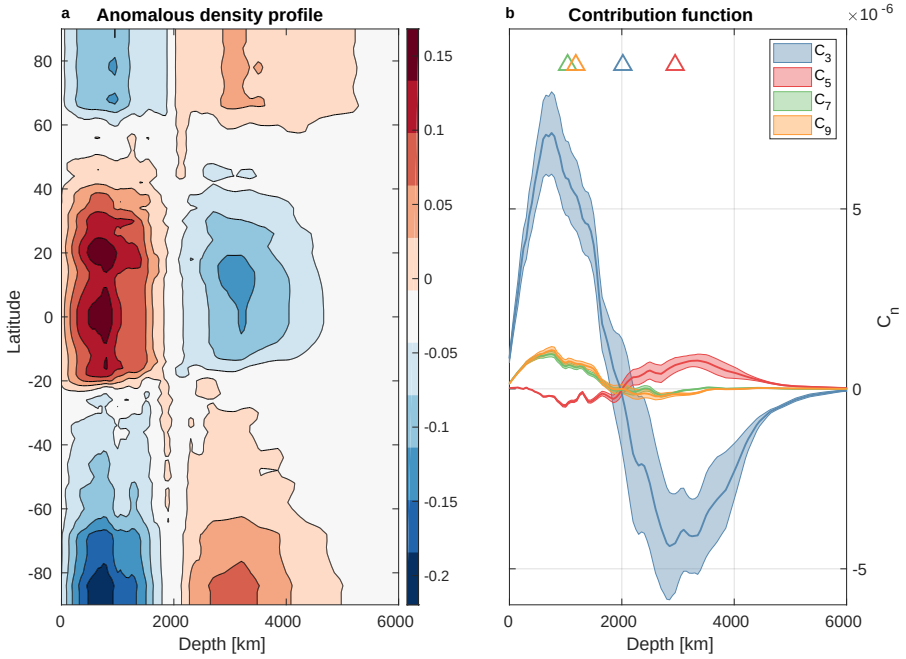

Figure 3: (a) The mean anomalous density profile of all possible decay options that fits the Juno four measured odd gravity harmonics, colors represent anomalous density values range [kg m^{-3}]. (b) Averaged contribution function (lines) for each of the odd gravity harmonics and the associated standard deviation (shading), triangles stand for the depth of mean anomaly. Both panels are for all the latitudes and only for the upper $\sim$ 6000 km, below this depth the anomalous density is near constant.

enough mass to affect the gravity field, and the cloud-level observed flow is limited to a shallow enough layer so it does not affect the gravity field.

The simplest case is clearly to use the measured profile at Jupiter's cloud-level and allow its magnitude to decay with depth (section 3). A slightly less constraining option is to insert a perturbation to the measured profile, therefore keeping the general form and allow a varying level of modifications to the cloud-level flow. The perturbed winds chosen here might represent the measured uncertainties in Jupiter's cloud-level wind (Garcıa-Melendo and Sánchez-Lavega, 2001; Tollefson et al., 2017). Finally, random meridional profiles of the zonal flow with a spectra generally similar to Jupiter's are examined as well.

The modified zonal flow structure is chosen at the cloud level and projected inwards along the rotation axis (u_{proj}, Eq. 4) with a range of vertical structures as described in section 3. The profiles are calculated by adding sine-like perturbations to the measured wind. The standard deviation for the perturbations in the modified profiles is $5 \pm 0.5\,\mathrm{m\ s^{-1}}$ (varies with latitudes), well within the measurement error (Garcıa-Melendo and Sánchez-Lavega, 2001; Tollefson et al., 2017). The perturbation is constructed as

$$\epsilon\left(\theta\right) = \sum_{n=1}^{10} \left[a_n \sin\left(2n\theta\right) + b_n \cos\left(2n\theta\right)\right], \tag{8}$$

where ϵ is the perturbation, a_n and b_n are random numbers that are normally distributed around zero with standard deviation of 2. We first examine 1000 modified profiles, where each profile is being constructed by adding the perturbation to the measured wind (4.1). In addition, 1000 random profiles are constructed purely from the functions ϵ, with a standard deviation of $30\,\mathrm{m\ s^{-1}}$. These profiles represent internal winds that are completely unrelated to the observed cloud-level winds (4.2).

4.1 Perturbed cloud-level wind profiles

The perturbed wind profiles (Fig. 4e, colors) result in a substantially bigger solutions envelope (Fig. 4a-d, gray) than the one from the measured zonal wind profile case, consistent with the fact that we allow a wider range of wind

profiles. Note that the overall shape has changed and that the flow can even vanish at ~ 2500 km. This might have an important implication since the initial time-dependent magnetic field results from Juno imply that the wind in those regions should be very weak (Duer et al., 2019; Moore et al., 2019). Also, even for the perturbed winds there are no solutions fitting at least three odd J_n, that vanishes above 2000 km. The depth sensitivity of each harmonic is less unique than the measured wind case. This reflects the fact that Fig. 4 is a combination of all the possible solutions from 1000 examined meridional wind structures. Overall J_3 still seems to be sensitive in deeper regions, but so does J_7. J_5 turns to be the most insignificant harmonic and J_9 does affect the depth range of $1500-2000$ km unlike the unperturbed wind case. The substantially larger area of solutions, however, does not manifested in more solutions relative to the examined cases. From 1000 examined profiles tested with the decay sample population each, only about 0.1% fit the anomalous gravity field compared to about 1% in the unperturbed case (Fig. 6, red and blue). This suggests that although other solutions exists for the cloud-level wind, it is likely that a structure that is similar to the projected observed cloud-level is indeed the structure in the deeper atmosphere of Jupiter.

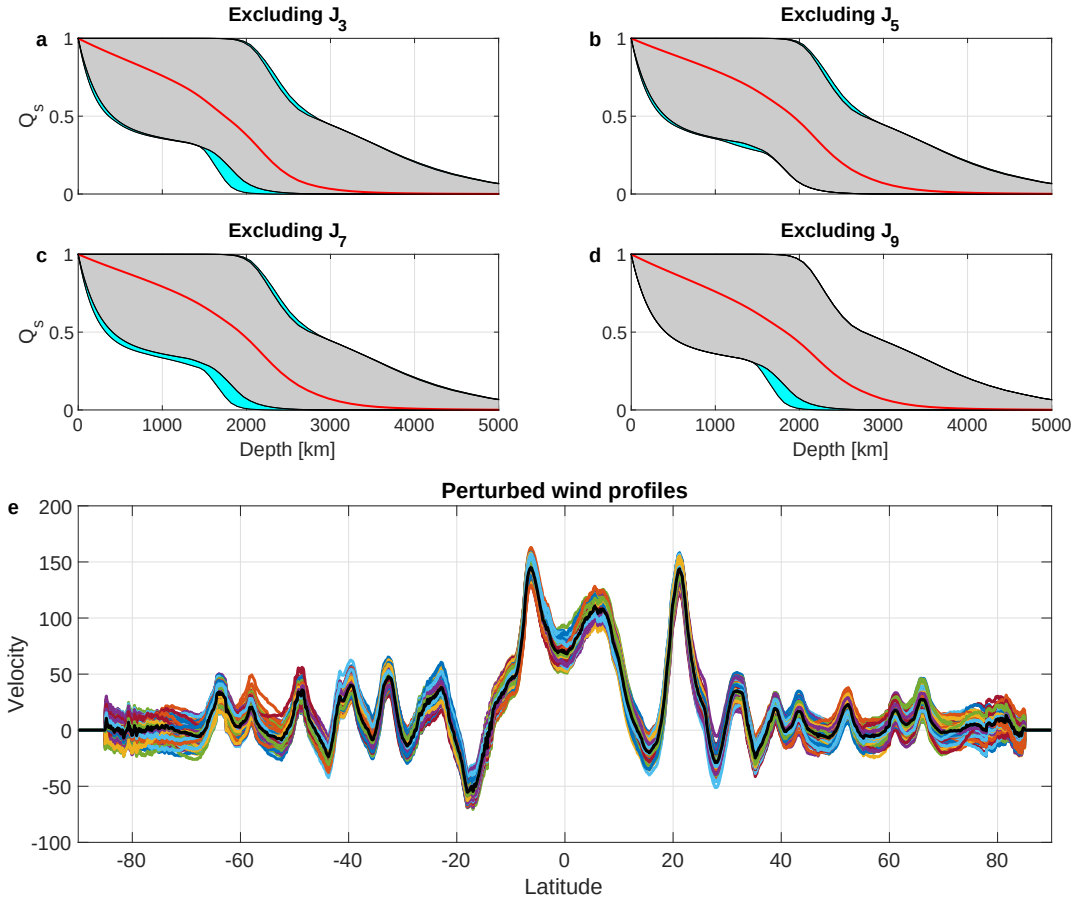

Figure 4: (a-d) Modified wind profiles odd gravity harmonics depth sensitivity summary as in Fig. 2 and (e) 100 examples of the 1000 profiles generated those odd harmonics values (colors, [m s^{-1}]) and Jupiter's measured wind profile (black). Each profile was examined with the same set of decay options. The results shown here are for all meridional and vertical options combined.

4.2 The possibility of other zonal wind profiles

Next, we consider profiles that do not resemble Jupiter's winds. The resulting solution envelopes of the random wind profiles are relatively similar to the previous case of perturbed winds (not shown). However, the ability of the 1000 examined random profiles, each with the sample of decay options, is considerably smaller than previous cases. Only about 0.01% fit all four odd gravity harmonics (Fig. 6, yellow). This clearly indicates that fitting all four odd numbers is difficult with random meridional profiles of zonal wind. Moreover, Only a very small subset of profiles (13 meridional arrangements out of 1000, about 1%) are able to fit with even a single decay profile the measured four values (Fig. 5a), and in general, the measured numbers do not appear to be coincidental with the

zonal flow structure. This should not come as a surprise since it is very unlikely that below the cloud level of Jupiter utterly different structure of zonal profile suddenly arise. Out of the 1000 random meridional profiles examined, combination of even two or more gravity harmonics is rare and exists in only 7% or less of the profiles (Fig. 5b,c).

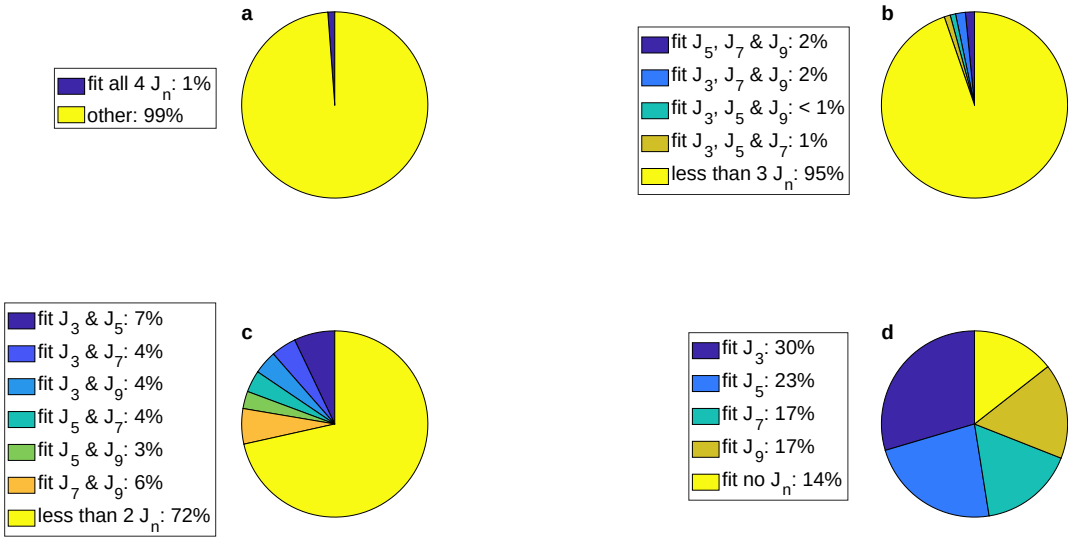

Figure 5: Summary of random meridional profiles correspondence to the odd gravity harmonics. Only $\sim 1\%$ of the zonal profiles are able to fit all four odd gravity harmonics (a), 10% of the zonal profiles fit at least three odd gravity harmonics (b), 45% of the zonal profiles fit at least two odd gravity harmonics (c) and 6% fit non of the odd gravity harmonics (d). The full compatibility distribution is detailed in the figure.

A summary of the examined cases appears in Fig. 6. Note that the ordinate is a logarithmic scale and that 100% stands for all the zonal profiles (1000 zonal wind profiles other than the measured wind) and all decay options (5×10^5) for each case. We find that the envelope of possible solutions from Fig. 1 stands for $\sim 1\%$ of the tested vertical structures for zonal flows. The fitting percentage decreases with increasing perturbations, and drops rapidly when switching to random profiles. This trend repeats for all variations of at least three odd harmonics. For all cases, the random winds shows significantly lower fitting percentage than the other cases. We further present fitting percentage of excluding two and three harmonics. Based on this section, we find that other meridional arrangements of the zonal wind are possible, but they are statistically unlikely. This result implies that the meridional structure of Jupiter's zonal winds is projected inwards and weakens with depth, and is likely not altered much from the cloud-level arrangement.

5 Zonal wind profiles inspired by the MWR measurements

An additional possible indication of whether the wind changes below the cloud level comes from Juno's six-channel microwave radiometer (MWR) measurement. The nadir brightness temperature (T_b) estimations calculated from the MWR measurements reveal a considerable variation in latitude and depth (Bolton et al., 2017) (Fig. 7a, black lines). The opacity of the atmosphere determines the brightness temperature, and in Jupiter, the main opacity source is ammonia (Li et al., 2017). Ingersoll et al. (2017) discuss a possible relation between the measured nadir brightness temperature and Jupiter's zonal jets, indicating that the latitudinal arrangement of the jets might be depth-dependent, in accordance with T_b, instead of simply projected inwards. The relation between the nadir brightness temperature and the zonal jets might be treated in two ways: the first, in which the measured brightness temperature is taken directly as temperature, in which case the relation to the wind shear would be through thermal wind balance as discussed in section 4. In this case, the equatorial wind would be greater by two orders of magnitude from the measured cloud-level wind (Bolton et al., 2017). The second way is to examine the possibility that the MWR measurements indirectly reflect the latitudinal variability of the wind beneath the cloud level. This relation might be manifested through the ammonia concentration as an indicator on the meridional circulation and this is connected to the zonal flows (as in Ferrel cells). Here, we choose to focus on the second option, by analyzing a range of depth-dependent meridional profiles, compatible with the nadir brightness temperature trends.

The MWR measurements appear to get smoother with depth from channel 6 (cloud-level) towards channel 1 ($\sim$ 300 km depth) (Fig. 7a, black lines). The most apparent feature of the nadir temperature in channel 1 is the

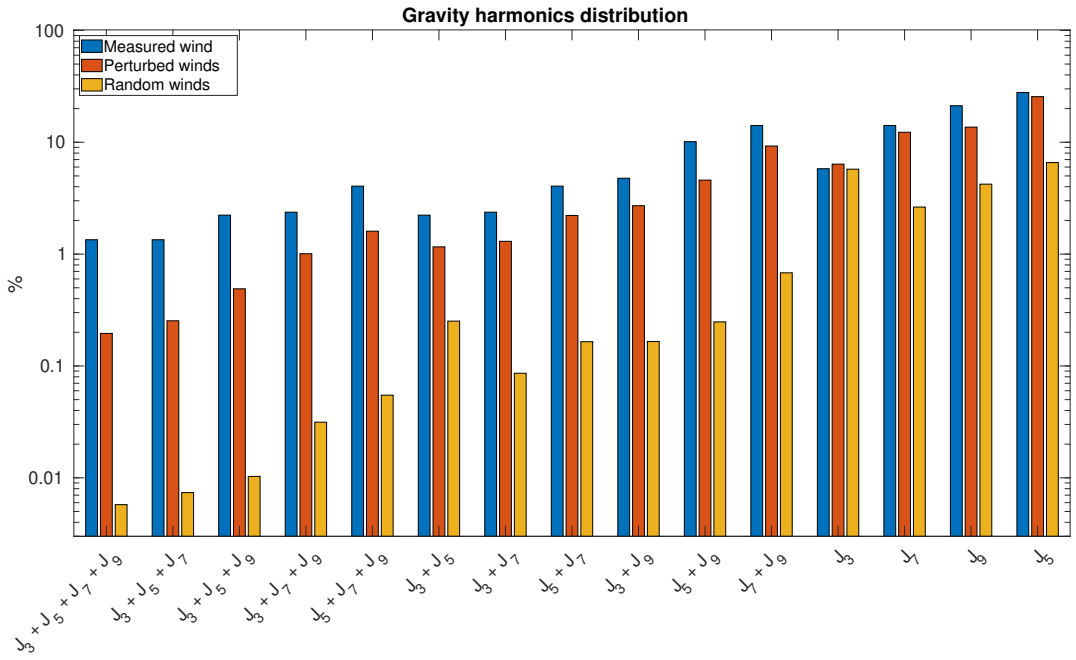

Figure 6: Solutions summary for the four presented cases of wind structures: Jupiter's measured wind at the cloud level (blue), 1000 slightly modified meridional structures (red) and 1000 random zonal profiles with similar general structure to Jupiter's zonal profile (yellow). The ordinate is a logarithmic scale of percentage relative to all cases that were examined. The particular requirement of the solution to match the different odd gravity harmonics is presented by the abscissa.

equatorial anomaly (Fig. 7b.1). Both Jupiter's meridional profile and the brightness temperature reveals alternating patterns at the cloud-level (channel 6) (Fig. 7b.6), yet the brightness temperature waviness vanishes in the deeper channels, most prominently in channel 1 (Fig. 7b.1). To address this behavior, we consider a range of modified cases, where in each we set the wind strength in the six channels according to MWR results and project the wind strength from channel 1 ($\sim$ 300 km) inwards. The wind at channel 1 is composed using a running average of $\Delta\theta$ degrees, where $\Delta\theta = 0, 1, 2, ..., 10$ (0 means that no running average is applied). Below the depth of 300 km we project the winds with no further assumptions. We then use the same set of decay functions as in previous cases to decay the wind strength with depth (section 3). The running average at depth allows matching between the temperature trend and the zonal jets. For comparison, three options for the deep winds are presented in 7. The first, without running average at depth ($\Delta\theta = 0°$), is not consistent with the nadir temperature trend at depth (Fig. 7b, light blue). The other two options, with increased smoothness of the zonal wind profile with depth, are more compatible with the nadir temperature (Fig. 7b, blue).

Although the latitudinal trend of the zonal jets and T_b seems to be related at channel 6 (Fig. 7a), the correlation between them is low (Tab. 1). However, the correlation increases with both increasing depth from channel 6 to channel 1, and with increasing running average ($\Delta\theta$). The high correlation at channel 1 between T_b and the modified zonal flow with $\Delta\theta = 8°$ (Tab. 1) strengthens the assumption that T_b should not be treated as actual temperature at this depth. Finally, we examine the correlation between the wind projected along the radial axis and T_b for the non modified case ($\Delta\theta = 0°$). We find that projecting the winds along the spin axis (cylindrical projection) (Fig. 7b.1, dashed gray) is slightly better correlated with the MWR data than projecting them along the radial axis (radial projection) (Tab. 1).

We next examine the ability of the smoothed profiles to explain the measured odd gravity harmonics. We examine a range of case studies, from slightly to largely modified depth dependent profile, until no solutions are found (Fig. 8a). For slightly smoother profiles, the ability to fit all four odd J_n is similar to that without any smoothing (Fig. 8a). Stronger smoothing leads to less ability to fit the odd four J_n. Using more than 10 degrees running average results in no solutions for the odd gravity harmonics. Comparison between the ability to fit the gravity harmonics, while excluding one of them, for the three case studied in Fig. 7, shows a steady tendency, with all the odd J_n affected by the relaxation until no solutions can be found (Fig. 8b). This result is compatible with the previous cases (sections 3 and 4), indicating that deep wind that resembles the cloud-level wind can fit the

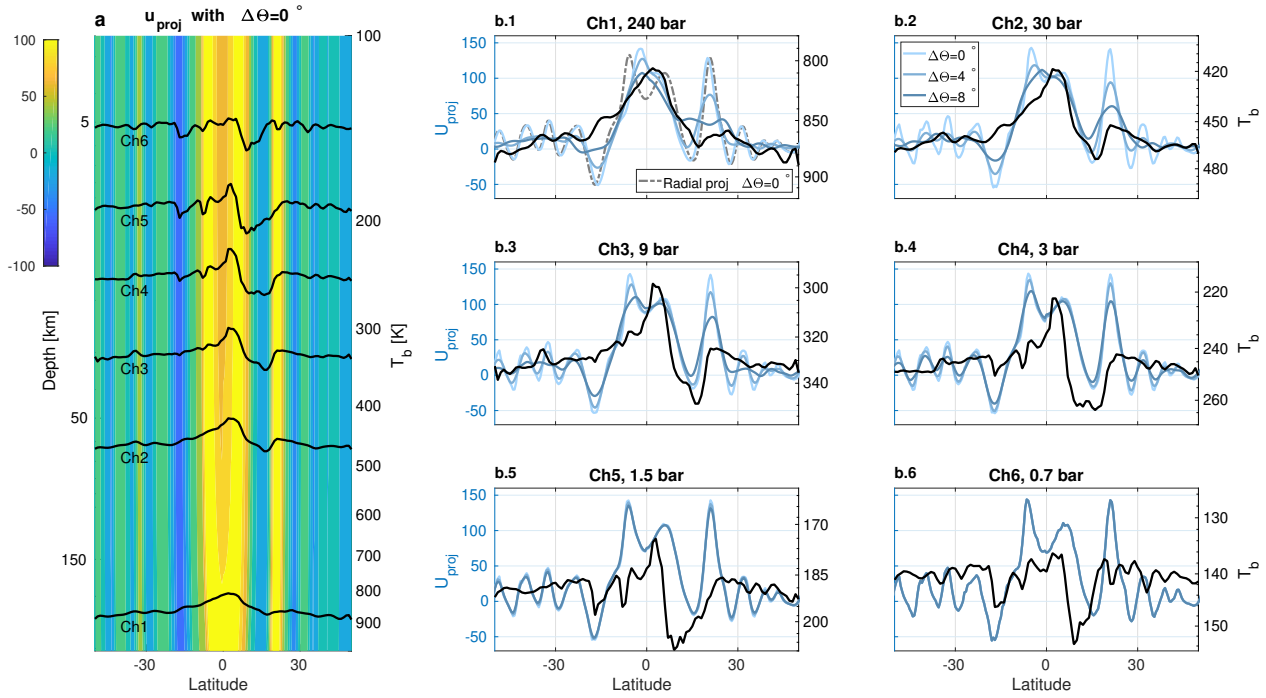

Figure 7: (a) Jupiter's projected wind velocities (colors, [m s^{-1}]) between latitudes $-50°$ and $50°$ in the upper 300 km of Jupiter (left ordinate) combined with nadir brightness temperature lines from Juno's PJ1 (black, right ordinate) in channels 1 to 6, associated with frequencies of 0.6, 1.2, 2.6, 5.2, 10 and 22 GHz, respectively. (b.1-6) Jupiter's projected wind velocities (m s^{-1}) at channel 1 , 240 bar (b.1), channel 2 , 30 bar (b.2), channel 3, 9 bar (b.3), channel 4, 3 bar (b.4), channel 5, 1.5 bar (b.5), and channel 6, 0.6 bar (b.6) for running average of $\Delta\theta = 0°$, $\Delta\theta = 4°$ and $\Delta\theta = 8°$ (darker blue with increasing $\Delta\theta$, left ordinate). Also shown is the brightness temperature (°K) (black, right ordinate). The radial projection of the winds with no running average (dashed gray) is also presented in b.1.

gravity data, while changing the zonal wind structure considerably limits the ability to find a solution.

6 Discussion and conclusions

The main challenge of interpreting the Juno gravity measurements is that the measurements provide only a handful of numbers (gravity harmonics), while the meridional and vertical profile of the interior flow have many degrees of freedom, and therefore by-definition the problem is ill-posed. Acknowledging this inherent issue, Kaspi et al. (2018) used four degrees of freedom for the vertical flow profile (matching the number of the four odd harmonics), and found the best optimized profile for this allowed range. They addressed the non-uniqueness by showing the statistical likelihood of wind profiles for the interior that are completely different than the cloud-level flow. Kong et al. (2018) highlighted the non-uniqueness issue by showing that two different flow profiles can still satisfy the gravity measurements. In this study we take a more methodological approach and consider a wider range of solutions and analyze their statistical likelihood. The flow profiles we consider, both for the meridional and vertical profiles, are bound by physical considerations. We also address two main issues: First, all previous studies looked at all four odd gravity harmonics together and found the flow profiles best matching all four. Here, we investigate how does each one of them separately bound the flow. Second, in attempt to coincide the gravity and microwave data, we explore if deep profiles that are smoother than those of the cloud level, as possibility indicated by the microwave nadir temperature measurements, can be consistent with the gravity measurements.

Beginning with assuming that the cloud-level wind profile is projected inwards parallel to the spin axis, with some decay profile, we identify the envelope of possible solutions (Fig. 1). We then relax the dependence on each of the odd gravity harmonics separately and by this analyze their individual contribution to the vertical profile of the zonal wind (Fig. 2). We find that J_3, which is the lowest order odd harmonic that represent the dynamics of Jupiter, is sensitive at depths where the conductivity rises (beyond ~ 3000 km) and the magnetic field might be interacting with the flow, resulting in the Lorentz force playing a key role in the dynamics. J_5 appears to be the most sensitive

Table 1: Correlation coefficients between T_b and the wind velocity at each channel, for winds projected in the radial direction (RP) with no running average ($\Delta\theta = 0°$), cylindrical projection along the spin axis (CP) with no running average ($\Delta\theta = 0°$), CP with running average of 4 degrees ($\Delta\theta = 4°$), and CP with running average of 8 degrees ($\Delta\theta = 8°$). Note that the correlation increase with depth (or decrease with channel) and with running average. Also correlation is higher for CP compared with RP when no running average is applied.

Channel	RP, $\Delta\theta = 0°$	CP, $\Delta\theta = 0°$	CP, $\Delta\theta = 4°$	CP, $\Delta\theta = 8°$
1	0.64	0.64	0.76	0.86
2	0.70	0.74	0.80	0.84
3	0.60	0.63	0.65	0.68
4	0.37	0.41	0.41	0.42
5	0.11	0.13	0.13	0.13
6	0.10	0.10	0.10	0.10

harmonic, giving a robust constraint on the vertical structure of the zonal flow alone (Fig. 2b). Interestingly, J_9 does not give any new constraint on the flow if the other three harmonics are within the sensitivity range (Fig. 2d). A possible explanation for J_5 unique nature comes from exploring the contribution function, revealing that J_5 is most sensitive in the deeper regions, below 2000 km (Fig. 3).

The modified zonal flows analysis revealed a substantially bigger possible solutions envelope than that with extending the cloud-level wind (Fig. 4). This implies that the depth sensitivity of each harmonic might alter with different structure of zonal wind, however, the overall structure remains similar. Even for the perturbed winds, the flow cannot vanish shallower than 2000 km depth. The case with random winds implies that, with high probability, the wind cannot alter completely below the cloud level. Fitting the four odd gravity harmonics (or three if we ignore J_9) is not coincidental and requires either similar winds to the measured ones that would penetrate few thousands of kilometers into the planet, or a very specific and statistically unlikely combination of meridional wind profile and a decay structure (Fig. 6). Finally, the gravity harmonics induced by the slightly modified depth-dependent meridional profiles, that are more compatible with the MWR measurements at depth (Fig. 7), are still within Juno's gravity measurements uncertainty, indicating that the nadir brightness temperature could indeed reflect on the structure of the zonal jet at 300 km (Fig. 8).

Acknowledgments:

We thank Cheng Li for providing the MWR data. This research has been supported by the Israeli Space Agency and the Helen Kimmel Center for Planetary Science at the Weizmann Institute of Science. Models used in this study are publicly available. The Juno gravity measurements (Iess et al., 2018) and MWR measurements (Li et al., 2017) are publicly available, see doi.org/10.1038/nature25776 and doi.org/10.1002/2017GL073159, respectively. Additional data can be found here https://doi.org/10.5281/zenodo.3684739.

References

Bolton, S. J., Adriani, A., Adumitroaie, V., Allison, M., Anderson, J., Atreya, S., Bloxham, J., Brown, S., Connerney, J. E. P., DeJong, E., Folkner, W., Gautier, D., Grassi, D., Gulkis, S., Guillot, T., Hansen, C., Hubbard, W. B., Iess, L., Ingersoll, A., Janssen, M., Jorgensen, J., Kaspi, Y., Levin, S. M., Li, C., Lunine, J., Miguel, Y., Mura, A., Orton, G., Owen, T., Ravine, M., Smith, E., Steffes, P., Stone, E., Stevenson, D., Thorne, R., Waite, J., Durante, D., Ebert, R. W., Greathouse, T. K., Hue, V., Parisi, M., Szalay, J. R., and Wilson, R. (2017). Jupiter's interior and deep atmosphere: The initial pole-to-pole passes with the Juno spacecraft. *Science*, 356:821–825.

Busse, F. H. (1976). A simple model of convection in the Jovian atmosphere. *Icarus*, 29:255–260.

Cao, H. and Stevenson, D. J. (2017). Zonal flow magnetic field interaction in the semi-conducting region of giant planets. *Icarus*, 296:59–72.

Duer, K., Galanti, E., and Kaspi, Y. (2019). Analysis of Jupiter's deep jets combining Juno gravity and time-varying magnetic field measurements. *Astrophys. J. Let.*, 879(2):L22.

French, M., Becker, A., Lorenzen, W., Nettelmann, N., Bethkenhagen, M., Wicht, J., and Redmer, R. (2012). Ab initio simulations for material properties along the Jupiter adiabat. *Astrophys. J. Sup.*, 202:5.

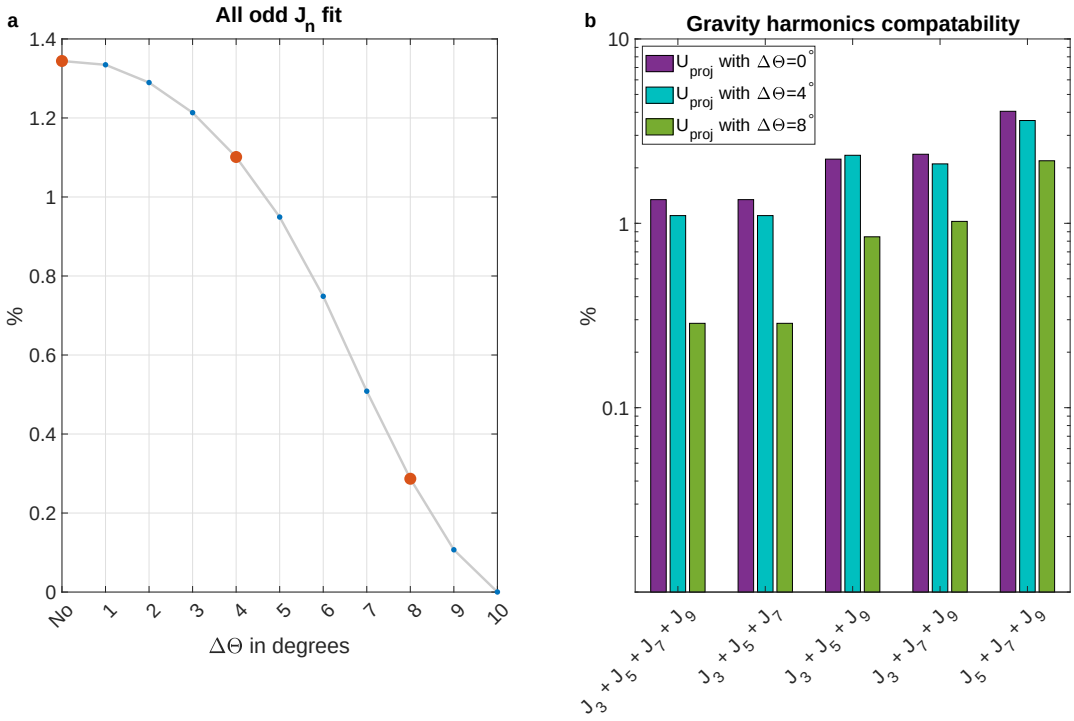

Figure 8: (a) The ability of the depth dependent wind profiles to fit all four odd gravity harmonics (percentage of solutions) as function of the smoothing factor in degrees (blue line). The three cases shown in Fig. 7b are denoted by red dots. (b) The gravity harmonics distribution for the red dots compatible to the three case studies in Fig. 7b. The ordinate is a scale of percentage relative to the 5×10^5 random decay options examined.

Galanti, E., Cao, H., and Kaspi, Y. (2017a). Constraining Jupiter's internal flows using Juno magnetic and gravity measurements. *Geophys. Res. Lett.*, 44:8173–8181.

Galanti, E., Kaspi, Y., and Tziperman, E. (2017b). A full, self-consistent, treatment of thermal wind balance on fluid planets. *J. Comp. Phys.*, 810:175–195.

Garcıa-Melendo, E. and Sánchez-Lavega, A. (2001). A study of the stability of jovian zonal winds from HST images: 1995–2000. *Icarus*, 152(2):316–330.

Gastine, T., Wicht, J., Duarte, L. D. V., Heimpel, M., and Becker, A. (2014). Explaining Jupiter's magnetic field and equatorial jet dynamics. *Geophys. Res. Lett.*, 41:5410–5419.

Guillot, T. and Gautier, D. (2007). *Treatise of Geophysics: 10. Planets and Moons*, chapter Giant planets, pages 439–464. Elsevier.

Guillot, T., Miguel, Y., Militzer, B., Hubbard, W. B., Kaspi, Y., Galanti, E., Cao, H., Helled, R., Wahl, S. M., Iess, L., Folkner, W. M., Stevenson, D. J., Lunine, J. I., Reese, D. R., Biekman, A., Parisi, M., Durante, D., Connerney, J. E. P., Levin, S. M., and Bolton, S. J. (2018). A suppression of differential rotation in Jupiter's deep interior. *Nature*, 555:227–230.

Helled, R., Anderson, J. D., Podolak, M., and Schubert, G. (2010). Interior models of Uranus and Neptune. *Astrophys. J.*, 726(1):15.

Hubbard, W. B. (1984). *Planetary Interiors*. pp. 343. New York, Van Nostrand Reinhold Co.

Hubbard, W. B. (1999). Note: Gravitational signature of Jupiter's deep zonal flows. *Icarus*, 137:357–359.

Hubbard, W. B. (2012). High-precision Maclaurin-based models of rotating liquid planets. *Astrophys. J. Let.*, 756:L15.

Hubbard, W. B., Slattery, W. L., and Devito, C. L. (1975). High zonal harmonics of rapidly rotating planets. *Astrophys. J.*, 199:504–516.

Hubbard, W. B., Trubitsyn, V. P., and Zharkov, V. N. (1974). Significance of gravitational moments for interior structure of Jupiter and Saturn. *Icarus*, 21(2):147–151.

Iess, L., Folkner, W. M., Durante, D., Parisi, M., Kaspi, Y., Galanti, E., Guillot, T., Hubbard, W. B., Stevenson, D. J., Anderson, J. D., Buccino, D. R., Casajus, L. G., Milani, A., Park, R., Racioppa, P., Serra, D., Tortora, P., Zannoni, M., Cao, H., Helled, R., Lunine, J. I., Miguel, Y., Militzer, B., Wahl, S., Connerney, J. E. P., Levin, S. M., and Bolton, S. J. (2018). Measurement of Jupiter's asymmetric gravity field. *Nature*, 555(7695):220–222.

Ingersoll, A. P., Adumitroaie, V., Allison, M. D., Atreya, S., Bellotti, A. A., Bolton, S. J., Brown, S. T., Gulkis, S., Janssen, M. A., Levin, S. M., Cheng, L., Liming, L., Lunine, J. I., Orton, G. S., Oyafuso, F. A., and Steffes, P. G. (2017). Implications of the ammonia distribution on Jupiter from 1 to 100 bars as measured by the Juno microwave radiometer. *Geophys. Res. Lett.*, 44(15):7676–7685.

Jones, C. A. and Kuzanyan, K. M. (2009). Compressible convection in the deep atmospheres of giant planets. *Icarus*, 204:227–238.

Kaspi, Y. (2013). Inferring the depth of the zonal jets on Jupiter and Saturn from odd gravity harmonics. *Geophys. Res. Lett.*, 40:676–680.

Kaspi, Y., Davighi, J. E., Galanti, E., and Hubbard, W. B. (2016). The gravitational signature of internal flows in giant planets: comparing the thermal wind approach with barotropic potential-surface methods. *Icarus*, 276:170–181.

Kaspi, Y., Flierl, G. R., and Showman, A. P. (2009). The deep wind structure of the giant planets: Results from an anelastic general circulation model. *Icarus*, 202:525–542.

Kaspi, Y., Galanti, E., Hubbard, W. B., Stevenson, D. J., Bolton, S. J., Iess, L., Guillot, T., Bloxham, J., Connerney, J. E. P., Cao, H., Durante, D., Folkner, W. M., Helled, R., Ingersoll, A. P., Levin, S. M., Lunine, J. I., Miguel, Y., Militzer, B., Parisi, M., and Wahl, S. M. (2018). Jupiter's atmospheric jet-streams extend thousands of kilometers deep. *Nature*, 555:223–226.

Kaspi, Y., Hubbard, W. B., Showman, A. P., and Flierl, G. R. (2010). Gravitational signature of Jupiter's internal dynamics. *Geophys. Res. Lett.*, 37:L01204.

Kong, D., Zhang, K., Schubert, G., and Anderson, J. D. (2018). Origin of Jupiter's cloud-level zonal winds remains a puzzle even after Juno. *Proc. Natl. Acad. Sci. U.S.A.*, 115(34):8499–8504.

Li, C., Ingersoll, A., Janssen, M., Levin, S., Bolton, S., Adumitroaie, V., Allison, M., Arballo, J., Bellotti, A., Brown, S., Ewald, S., Jewell, L., Misra, S., Orton, G., Oyafuso, F., Steffes, P., and Williamson, R. (2017). The distribution of ammonia on Jupiter from a preliminary inversion of Juno microwave radiometer data. *Geophys. Res. Lett.*, 44(11):5317–5325.

Liu, J., Goldreich, P. M., and Stevenson, D. J. (2008). Constraints on deep-seated zonal winds inside Jupiter and Saturn. *Icarus*, 196:653–664.

Moore, K. M., Cao, H., Bloxham, J., Stevenson, D. J., Connerney, J. E., and Bolton, S. J. (2019). Time-variation of Jupiter's internal magnetic field consistent with zonal wind advection. *Nature Astronomy*, page 1.

Nellis, W. J., Mitchell, A. C., McCandless, P. C., Erskine, D. J., and Weir, S. T. (1992). Electronic energy gap of molecular hydrogen from electrical conductivity measurements at high shock pressures. *Phys. Rev. Let.*, 68(19):2937.

Nellis, W. J., Weir, S. T., and Mitchell, A. C. (1996). Metallization and electrical conductivity of hydrogen in Jupiter. *Science*, 273(5277):936–938.

Nettelmann, N., Helled, R., Fortney, J. J., and Redmer, R. (2013). New indication for a dichotomy in the interior structure of Uranus and Neptune from the application of modified shape and rotation data. *Planatary and Space Science*.

Nettelmann, N., Püstow, R., and Redmer, R. (2013). Saturn layered structure and homogeneous evolution models with different eoss. *Icarus*, 225(1):548–557.

Pedlosky, J. (1987). *Geophysical Fluid Dynamics*. pp. 710. Springer-Verlag.

Salyk, C., Ingersoll, A. P., Lorre, J., Vasavada, A., and Del Genio, A. D. (2006). Interaction between eddies and mean flow in Jupiter's atmosphere: Analysis of Cassini imaging data. *Icarus*, 185:430–442.

Showman, A. P. and Kaspi, Y. (2013). Atmospheric dynamics of brown dwarfs and directly imaged giant planets. *Astrophys. J.*, 776:85–103.

Tollefson, J., Wong, M. H., de Pater, I., Simon, A. A., Orton, G. S., Rogers, J. H., Atreya, S. K., C., R. G., Januszewski, W., Morales-Juberías, R., and S., M. P. (2017). Changes in Jupiter's zonal wind profile preceding and during the Juno mission. *Icarus*, 296:163–178.

Weir, S. T., Mitchell, A. C., and Nellis, W. J. (1996). Metallization of fluid molecular hydrogen at 140 GPa (1.4 mbar). *Phys. Rev. Let.*, 76:1860–1863.

Wicht, J., Gastine, T., and Duarte, L. D. (2019a). Dynamo action in the steeply decaying conductivity region of Jupiter-like dynamo models. *J. Geophys. Res. (Planets)*, 124(3):837–863.

Wicht, J., Gastine, T., Duarte, L. D., and Dietrich, W. (2019b). Dynamo action of the zonal winds in Jupiter. *Astron. and Astrophys.*, 629:A125.

Zharkov, V. N. and Trubitsyn, V. P. (1974). Determination of the equation of state of the molecular envelopes of Jupiter and Saturn from their gravitational moments. *Icarus*, 21(2):152–156.